**GSA Data Repository 2016028**

**Nanoscale constraints on porosity generation and fluid flow during serpentinization**

Benjamin M. Tutolo, David F.R. Mildner, Cedric V.L. Gagnon, Martin O. Saar, and William E. Seyfried, Jr.

## EXTENDED METHODS SECTION

Samples were prepared as doubly polished, 150 μm thick sections mounted to quartz glass slides by Burnham Petrographics, LLC to reduce unwanted multiple scattering (Anovitz et al., 2009). Rectangular and circular neutron-absorbing Cd apertures were used to isolate individual regions of samples; a 22.2 mm x 3 mm and a 22.2 mm x 2 mm rectangular aperture (10 and 6.7 $mm^3$ measured volume, respectively) were used to isolate regions within the Atlantis

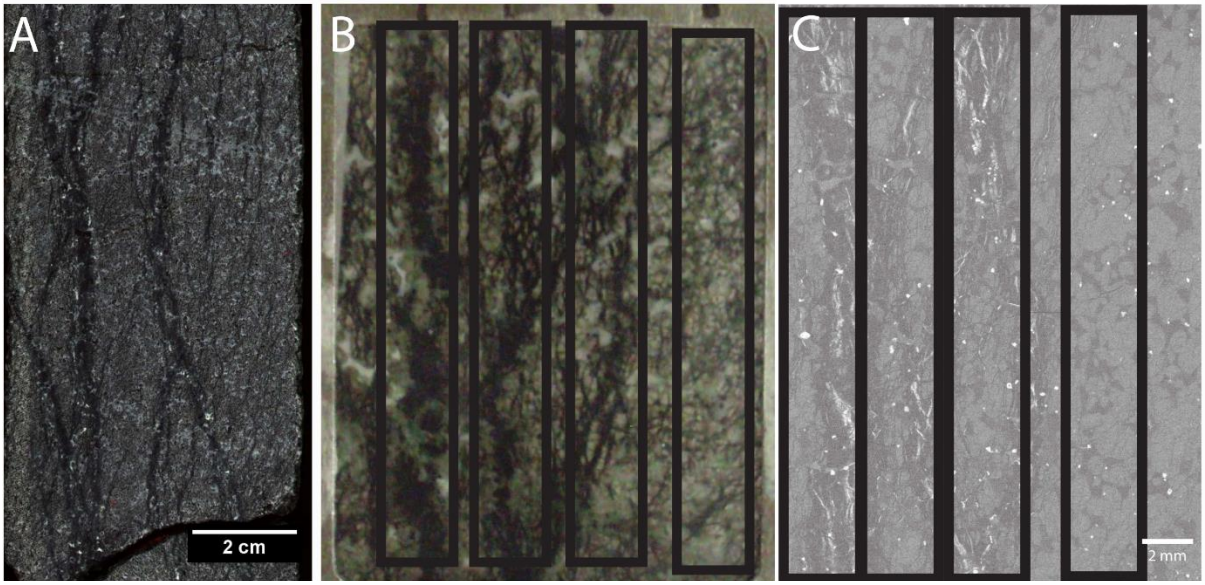


Figure DR1 Images of Atlantis Massif sample U1309D-235-R2-W-28-31, which was analyzed using neutron scattering. (A) High resolution photograph of the recovered core section (Blackman et al., 2006). (B) Thick section sample prepared for neutron scattering measurements. Box outlines indicate the regions of the sample that were analyzed in individual measurements. From right to left, they are regions 1, 2, 3, and 4. (C) X-ray computed tomography image of the billet from which the thick section in (B) was cut. Mineral abundances for use in calculation of the neutron scattering length densities of the individual analyses were calculated by segmenting the grayscale within this image.

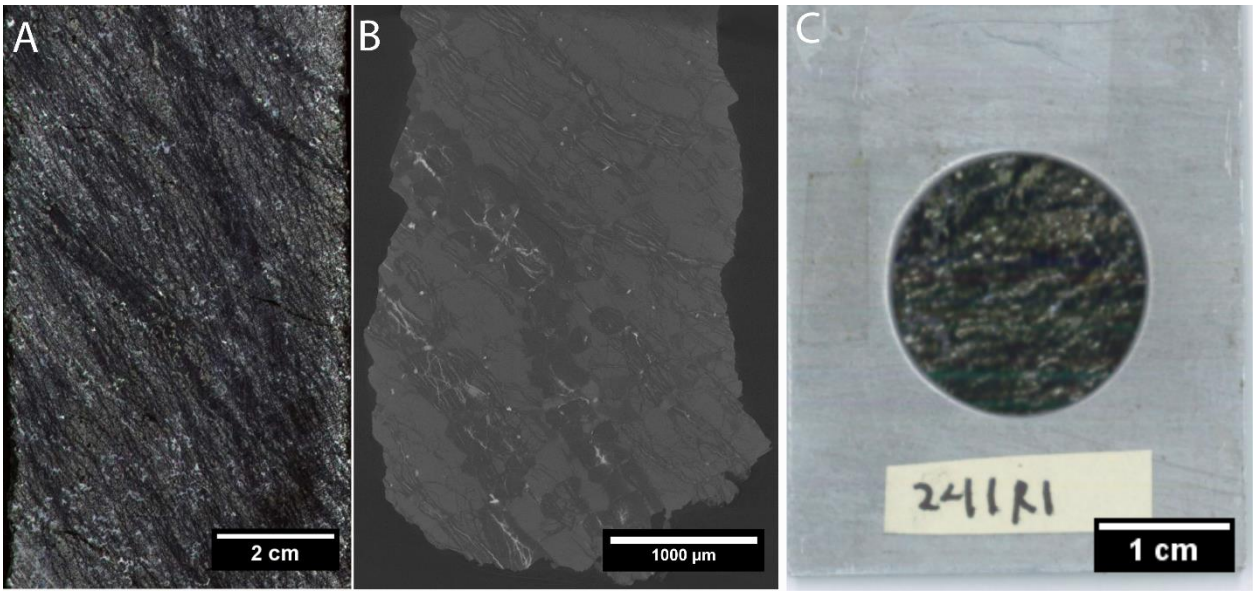


Figure DR2 Images of Atlantis Massif sample U1309D-241-R1-W-13-17, which was analyzed using neutron scattering. (A) High resolution photograph of the recovered core section (Blackman et al., 2006). (B) X-ray computed tomography image of a subsample acquired from the recovered core (note scale). (C) Thick section sample prepared for neutron scattering measurements, showing the gray circular Cd aperture.

Massif and Duluth Complex samples, respectively (Fig. DR1-DR3). Circular aperture size for whole-sample analyses of 235R2 and "Wall Rock + Fracture" was 9.53 mm (11 mm3 measured volume) and for 241R1 and the fractured Duluth Complex sample was 12.7 mm (19 mm3 measured volume) (Figs. DR1-DR3).

Neutron scattering length density (SLD) is a function of both elemental composition and density, and, unlike with X-ray scattering, is not an intuitive function of atomic number. Indeed, isotopes of the same element (e.g., $^{1}H$ and $^{2}H$) can have dramatically differing SLDs. In the present study, the NCNR SLD calculator (https://www.ncnr.nist.gov/resources/activation/) was used to calculate SLD as a function of chemical composition and density (Table DR1). X-

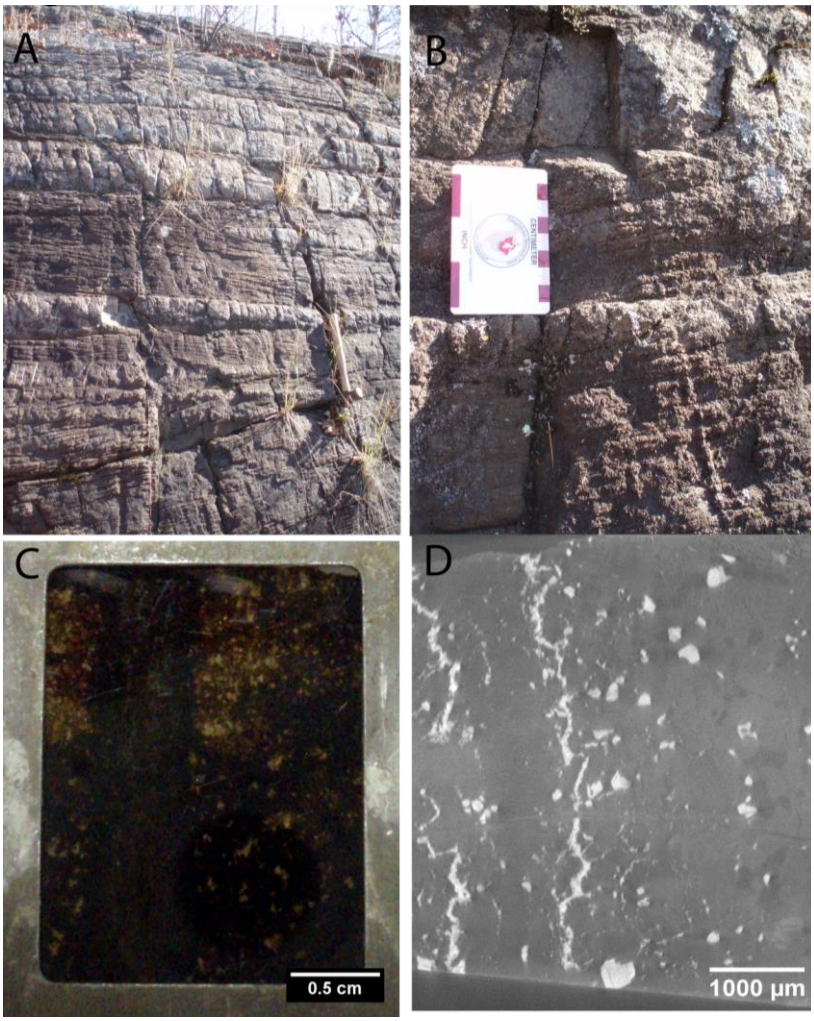


Figure DR3 Images of serpentinized samples from the Bardon Peak outcrop of the Duluth Complex. (A) Image of the full outcrop showing the "fracture cleavage" structure described by Foster and Hudleston (1985), with rock hammer for scale. (B) Image of the individual sample acquired for neutron scattering measurements (C) Thick section sample prepared for neutron scattering measurements. Individual measurements were performed in relation to the fracture present on the left side of the sample (D) X-ray computed tomography image of a subsample of the sample from which the thick section was prepared, illustrating the width and structure of the vein, wall rock and matrix.

ray computed tomography (XRCT), electron microprobe, inductively coupled plasma–optical emission spectroscopy and petrographic measurements and imaging were performed at the University of Minnesota (USA) and scanning electron microscope-energy dispersive spectrometry was performed at the University of Oxford (UK). Additional bulk rock and mineral phase chemical analyses were taken from Blackman et al. (2006) and Beard et al. (2009), respectively (Table DR1). To calculate the SLD of the Atlantis Massif samples, we utilized X-Ray Computed Tomography scans of the billet from which the relevant thick sections were cut. The images were segmented into 3 grayscale ranges using ImageJ (Abràmoff et al., 2004) : 1) Olivine; 2) Oxides; 3) Serpentine + Plagioclase. Visual analyses and calculations based on these

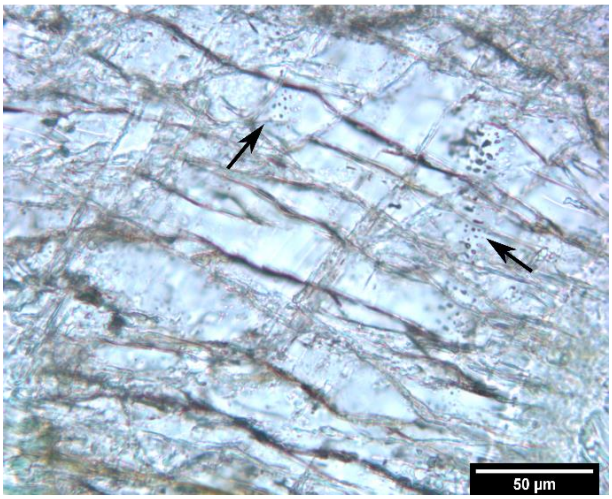


Figure DR4 Photomicrograph demonstrating fluid inclusions within IODP thin (30 µm) section U1309D #579, which was sampled just above sample 235R2. Fluid inclusions likely contribute to the porosities calculated from the neutron scattering curves.

segmented ranges were used to infer the approximate modal abundance of alteration phases within the analyzed regions. Electron microprobe analyses of olivine (Fo83) and plagioclase (An77) reported in Table DR1were used directly in the SLD calculation. For "oxides", magnetite formula and density were used because segmented sections of the least altered peridotite indicate that the pristine peridotite had very little (< 1 %) igneous oxides. For the "Serpentine + Plagioclase", the calculated SLD of serpentine was used because visual inspection indicates that it is dominantly composed of serpentine and the SLDs for these two minerals are in fact quite similar (Table DR1). Plagioclase solid solution densities were calculated as a linear interpolation between the values reported by Robie and Hemingway (1995) and olivine solid solution densities were calculated according to the equation presented by Bloss (1952). SLD for the Duluth Complex samples were calculated in a similar way. The bulk density of Duluth Complex troctolitic rocks was set to the value reported by Chandler (1990), 2.91 g/cm$^3$. SLD of pores within the sample were assumed to be equivalent to the SLD of air, ~0, although some of the pores may in fact be fluid inclusions, in which case the SLD would be ~ $-0.561\times10^{-6}$ Å$^{-2}$. In this case, the SLD contrast between pores and solids would be slightly greater (at most ~10%), and the calculated porosities and SSAs would be proportionally smaller. Calculated SLDs for our samples as well as relevant minerals and fluids are presented in Table DR1.

| Table DR1 Chemical analyses and neutron scattering length densities of relevant drill core samples from IODP borehole 1309D, hand sample from Bardon Peak, and analyzed regions of the samples. | | | | | | | | | | | | | | | | | | | | | | |
|---|---|---|---|---|---|---|---|---|---|---|---|---|---|---|---|---|---|---|---|---|---|---|
| **Sample** | **Depth** | **$SiO_2$** | **$TiO_2$** | **$Al_2O_3$** | **$Fe_2O_3$*** | **FeO** | **MnO** | **MgO** | **CaO** | **$Na_2O$** | **$K_2O$** | **$P_2O_5$** | **NiO** | **Cl** | **$CO_2$** | **$H_2O$** | **Total** | **Density** | **SLD** | **n** | **Method** | **Reference** |
| | **(mbsf)** | **(wt %)** | **(wt %)** | **(wt %)** | **(wt %)** | **(wt %)** | **(wt %)** | **(wt %)** | **(wt %)** | **(wt %)** | **(wt %)** | **(wt %)** | **(wt %)** | **(wt %)** | **(wt %)** | **(wt %)** | **(wt %)** | **($g/cm^3$)** | **($10^{-6}$ $Å^{-2}$)** | | | |
| Bardon Peak- Whole Rock | - | 36.37 | n.d | 4.97 | 27.90 | - | 0.28 | 18.92 | 3.03 | 0.40 | 0.08 | 0.04 | - | - | - | 7.29 | 99.28 | 2.91 | 4.11 | - | ICP-OES | This study |
| Olivine (Fo83) | - | 40.43 | 0.02 | 0.01 | - | 15.69 | 0.25 | 43.44 | 0.07 | n.d. | n.d. | n.d. | 0.19 | - | | - | 100.07 | 3.41 | 5.35 | 4 | EMP | Blackman |
| Olivine (Fo64) | - | 36.44 | | 0.01 | - | 31.15 | 0.43 | 31.53 | 0.08 | n.d. | - | - | 0.10 | - | - | - | 99.75 | 3.63 | 5.48 | 5 | EMP | This Study |
| Plagioclase (An76) | - | 49.21 | 0.04 | 32.53 | 0.28 | | 0.01 | 0.06 | 15.62 | 2.68 | 0.01 | - | | - | - | - | 100.44 | 2.73 | 3.97 | 5 | EMP | Blackman et al. (2006) |
| Plagioclase (An58) | - | 53.23 | - | 30.30 | - | 0.43 | n.d. | 0.04 | 11.46 | 4.58 | - | - | n.d. | - | - | - | 100.04 | 2.70 | 3.97 | 5 | EMP | this Study |
| Serpentine (Mg 96) | - | 40.80 | - | 0.96 | - | 3.12 | 0.05 | 40.14 | - | - | 0.23 | - | - | 0.23 | - | - | 85.53 | 2.73 | 3.78 | 73 | EMP | Beard et al. (2009) |
| Chlorite | - | 33.06 | - | 16.23 | - | 7.28 | 0.15 | 29.61 | 0.06 | - | - | - | - | 0.08 | - | - | 86.47 | 2.63 | 3.74 | 21 | EMP | Beard et al. (2009) |
| Serpentine + Brucite | - | 37.01 | - | 0.37 | - | 6.92 | 0.06 | 40.10 | - | - | - | - | - | 0.27 | - | 15.27 | 100.00 | 2.55[c] | 3.70 | 9 | EMP | Beard et al. (2009) |
| Prehnite | - | 43.39 | | 24.83 | 0.50 | - | 0.09 | 0.03 | 26.50 | 0.08 | 0.00 | - | - | 0.00 | - | 4.58 | 100.00 | 2.92 | 4.08 | 8 | EMP | Beard et al. (2009) |
| Bardon Peak fracture fill | - | 33.61 | - | 12.47 | - | 13.29 | 0.15 | 28.20 | 0.16 | 0.01 | - | - | - | 0.01 | | | 88.01 | 2.73 | 3.76 | 3 | EMP | This Study |
| Magnetite | - | | | | 68.97 | 31.03 | | | | | | | | | | | 31.03 | 5.15 | 6.91 | - | - | Ideal |
| Brucite | | | | | | | | 58.32 | | | | | | | | 30.89 | | 2.37 | 2.95 | | - | Ideal |
| Water | - | - | - | - | - | - | - | - | - | - | - | - | - | - | - | 100.00 | 100.00 | 1.00 | -0.56 | - | - | Ideal |
| 234R2 | 1126.83 | 38.98 | 0.07 | 3.99 | 12.11 | - | 0.17 | 34.44 | 3.42 | 0.26 | 0.01 | n.d. | - | - | 0.13 | 5.60 | 99.18 | 3.09 | 4.56 | - | ICP-AES | Blackman et al. (2006) |
| 241R1 | 1158.43 | 37.30 | n.d | 5.16 | 11.45 | - | 0.18 | 35.30 | 2.57 | 0.16 | 0.02 | 0.01 | - | - | 0.13 | 7.68 | 99.96 | 2.88 | 4.23 | - | ICP-OES | This Study |
| Fracture Core | - | 44.18 | n.d | 5.08 | - | 16.80 | 0.23 | 22.80 | 3.62 | n.d. | n.d. | n.d. | - | - | - | 7.29 | 100.01 | 2.91 | 4.21 | - | EDS Map | This study |
| Fracture Wall | - | 39.79 | 0.29 | 4.94 | - | 22.83 | n.d. | 19.45 | 5.40 | n.d. | n.d. | n.d. | - | - | - | 7.29 | 100.00 | 2.91 | 4.14 | - | EDS Map | This study |
| Matrix | - | 37.62 | 0.32 | 7.89 | - | 22.45 | 0.35 | 20.09 | 2.73 | n.d. | n.d. | n.d. | - | - | - | 7.29 | 100.00 | 2.91 | 4.12 | - | EDS Map | This study |
| | | | | | | | | | | | | | | **Serpentine + Plagioclase** | | **Olivine** | **Oxides** | | | | | |
| | | | | | | | | | | | | | | **(vol %)** | | **(vol %)** | **(vol %)** | | | | | |
| 235R2- Region 1 | | | | | | | | | | | | | | | 15 | 84 | 1 | 3.32[b] | 5.13 | | | |
| 235R2 - Region 2 | | | | | | | | | | | | | | | 47 | 48 | 5 | 3.18[b] | 4.69 | | | |
| 235R2 - Region 3 | | | | | | | | | | | | | | | 44 | 53 | 3 | 3.16[b] | 4.71 | | | |
| 235R2 - Region 4 | | | | | | | | | | | | | | | 57 | 36 | 6 | 3.12[b] | 4.53 | | | |

[a] $H_2O$ content for 241R1 And Bardon Peak was calculated from the measured LOI. In the case of the IODP samples, the average of the $CO_2$ contents measured for the tabulated IODP samples was subtracted from the measured LOI.

[b] Densities reported for the "subsamples" are approximate densities calculated from the mineral distribution

[c] Average of serpentine and brucite densities.

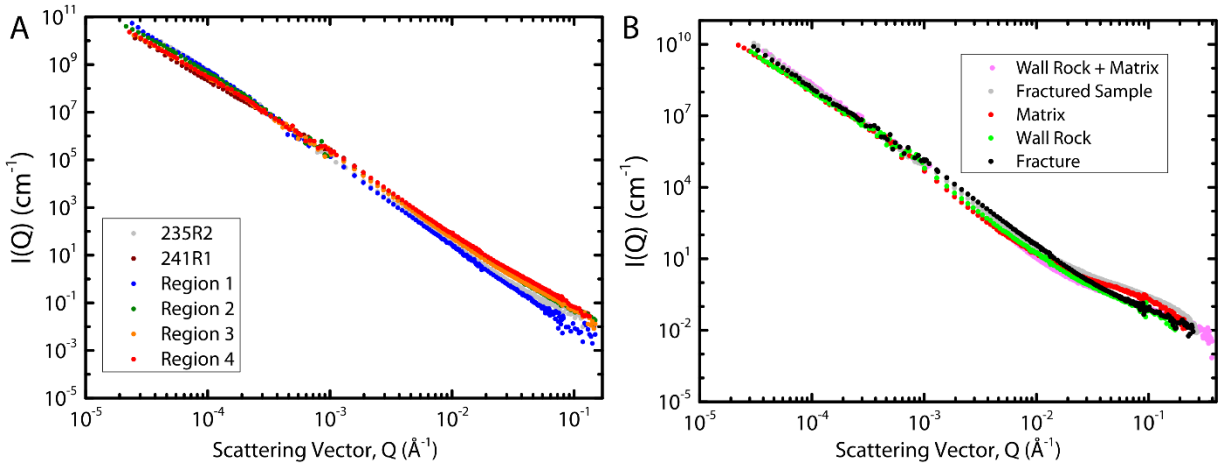


Figure DR5 Scattering intensity plotted on an absolute scale as a function of the scattering vector (Q) for the Atlantis Massif (A) and Duluth Complex samples (B). These plots are analogous to Fig. 2A and B in the text, which are plotted on a relative scale.

In general, the SLD contrast between the individual minerals are much smaller than the SLD contrast between samples and air. The only mineral-mineral contact with an SLD contrast similar to that of the rock-pore interfaces is that of magnetite-serpentine interfaces. This is a relevant mineral pairing, unlike, for example, olivine-magnetite contacts which are rare and generally separated by a layer of serpentine/brucite. However, magnetite-serpentine interfacial contacts are necessarily very small (i.e., in the nanometer range), both because of the diminutive size of the magnetite grains and because of the nature of the serpentine mineral structure (i.e., stacked, ~nm-sized sheets). Because neutron scattering is a scale-sensitive process, we would expect the scattering from magnetite-serpentine interfaces to occur in the high Q region of the SANS measurements, which does not appear to be systematically offset in the Atlantis Massif scattering curves.

The Duluth Complex samples show uncharacteristic slope of (U)SANS curves at high Q (>$10^{-2}$ Å$^{-1}$, representative of pores under ~10 nm in size, Figs. DR5, DR6), which suggests that scattering in this region is affected either by nm-scale ordering or scattering at mineral-mineral interfaces. It would potentially be possible to separate these effects by combining the presented

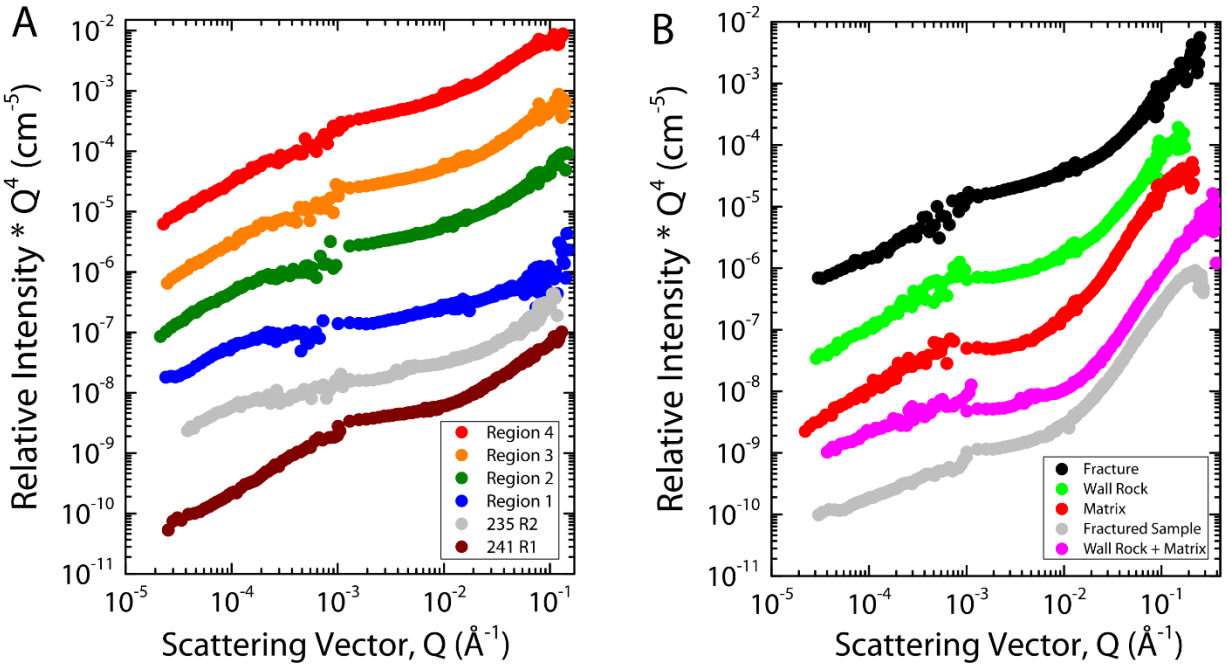


Figure DR6 Semi-Porod transforms of the Atlantis Massif (A) and Duluth Complex (B) (U)SANS curves. By multiplying the relative intensity by Q4, the variability within and between data sets as a function of Q may be examined in more detail. Note the uncharacteristically steep upward slope in the Duluth Complex samples above Q ≈ 10-2 Å-1, which is possibly due to nm-scale ordering or scattering at mineral-mineral interfaces. Data in this range were not used in the calculation of SSA as a function of probe size (Fig. 2).

USANS analysis with X-ray scattering analysis (Radlinski et al., 2004), but the ability to discern this high Q feature is not fundamentally important to the present study, and we therefore removed this data from the SSA and porosity analysis. The invariant calculation (see below) is much more sensitive to scattering at low Q (i.e., the USANS range), and therefore the effect from this anomalous region on the Duluth Complex measurements probably contributes negligibly to the results presented in Table 1.

The pore size distribution and SSA fitting in PRINSAS are described in detail in Hinde (2004) and Radlinski et al. (2004), but we give a brief summary of the procedure here. SSA in rocks, which have pores covering multiple length scales, is a function of the size of the probe

used for the measurement (e.g., Radlinski et al., 2004). A generalized model of the pore size distribution can be expressed as a histogram (Hinde, 2004):

$$I(Q) = \sum_i IQ_{0i} \frac{\int_{R_{min,i}}^{R_{max,i}} V_r^2 F_{sph}(Qr) dr}{(R_{max,i} - R_{min,i})}, \quad \text{(DR1)}$$

where I is the scattering intensity as a function of the scattering vector, $Q$; $R_{max,i}$ and $R_{min,i}$ are the boundaries of the *ith* histogram cell; $V_r = \frac{4\pi r^3}{3}$ is the volume of an individual, spherical pore; $F_{sph}(Qr)$ is the form factor for a sphere of radius r:

$$F_{sph}(Qr) = \left[3 \frac{\sin(Qr) - Qr\cos(Qr)}{(Qr)^3}\right]^2, \quad \text{(DR2)}$$

and $IQ_{0i}$, the contribution of the *ith* histogram cell, is:

$$IQ_{0i} = \frac{\Delta SLD^2 \phi}{\overline{V_r}} f(r_i)(R_{max,i} - R_{min,i}) \quad \text{(DR3)}$$

where $\phi$ is porosity, $\Delta SLD$ is the rock-pore SLD contrast, and $\overline{V_r} = \int_0^\infty V_r^2 f(r) dr$ is the average pore volume, and $f(r_i)$ is the probability density of the pore size distribution for the *ith* histogram cell. PRINSAS fits Eqn. (DR1) to the measured $I(Q)$, and then calculates specific surface area (SSA) as a function of probe of radius $r$ according to:

$$SSA(r) = n_v \int_r^{Rmax} A_r f(r') dr' \quad \text{(DR4)}$$

where $n_v$, the average number of pores per unit volume is:

$$n_v = \frac{\phi}{V_r} = \frac{I(0)}{\Delta SLD^2} \frac{1}{\overline{V_r^2}} \quad \text{(DR5)}$$

and *SSA(r)* is the total surface area of all pores with radius greater than $r$ ($A_r = \pi r^2$) normalized by the sample volume. Unfortunately, as designed, the fitting functions that PRINSAS employs do not guarantee that a global minimum has been reached nor do they allow for the estimation of errors associated with the solution that it returns (Hinde, 2004). Nevertheless, PRINSAS has been extensively verified against independent measurements performed with the more conventional gas sorption and mercury intrusion methods (e.g., Hinde, 2004; Radlinski et al, 2004; Navarre-Sitchler et al; 2013; Clarkson et al. 2013). In most cases within the present study, the fitted pore size distributions returned by PRINSAS using its standard fitting procedures were relatively smooth curves characteristic of those that may be expected for rocks. In some cases, the calculated *f(r)* distribution remained noisy even through the PRINSAS procedure of flattening and re-fitting the histogram curve; this could be reflective of the PRINSAS fitting procedure or noise in the (U)SANS data – similar results have been reported by others (Clarkson et al., 2013). Because calculations of *SSA(r)* represent the sum of the surface area of all pores with radii greater than the chosen probe radius, they lessen the contribution of any individual fitted point on the *f(r)* curve to the calculated curve, and thereby allow trends within the data to be more easily discerned. Indeed, calculated *SSA(r)* curves tend to vary little for a given sample, regardless of efforts to thin or smooth noisy data and improve the *f(r)* fit. The calculated curves are considerably more influenced by the sample's SLD. As noted in the text and observed in Eqns. DR3, DR4, and DR5, the calculated SSAs place the individual measurements on a common, familiar, geologically relevant unit scale ($m^{-1}$) and therefore permit comparison between individual measurements and with literature SSA analyses. Both the calculated *f(r)* and *SSA(r)* curves are given in the data repository spreadsheet associated with Fig. 2.

**Table DR2 Density and porosity measurements performed on relevant sections of IODP borehole 1309D (Blackman et al., 2006)**

| Sample | Depth (mbsf) | Density ($g/cm^3$) | n | Porosity (%) | n |
|---|---|---|---|---|---|
| 234R3 | 1128.41 | 3.066 | 1 | 0.3 | 1 |
| 235R1 | 1130.24 | 3.09 | 1 | 0.2 | 1 |
| 236R1 | 1134.86 | 2.88 | 1 | 0.6 | 1 |
| 240R2 | 1155.51 | 2.923 | 1 | 0.6 | 1 |
| 241R1 | 1158.44 | 2.884 | 1 | 0.4 | 1 |
| 242R1 | 1163.95 | 3.039 | 1 | 0.5 | 1 |
| "Olivine/Troctolititc Gabbro" | - | 2.91 ± 0.09 | 135 | 1.1 ± 0.9 | 130 |
| "Troctolite" | - | 2.84 ± 0.09 | 18 | 1.3 ± 0.5 | 17 |
| "Olivine-rich Troctolite" | - | 2.93 ± 0.16 | 31 | 0.9 ± 1.1 | 31 |
| "Peridotite" | - | 2.74 ± 0.04 | 3 | 2.0 ± 1.3 | 3 |

Porosity ($\phi$) may also be calculated from the invariants ($Y$) of scattering curves, according to:

$$Y \equiv \int_0^\infty Q^2\, I(Q) dQ = 2\pi^2 (\Delta SLD)^2 \phi(1-\phi), \qquad \text{(DR6)}$$

where $Q$ is the scattering vector, $I(Q)$ is the absolute scattering intensity, and $\Delta SLD$ is the rock-pore SLD contrast. Due to the lack of a known model for extrapolations to high and low Q, the values of $\phi$ that we present are representative of only those pores within the measured range. The disagreement between porosity calculated from the neutron scattering curves and those recorded onboard IODP leg 305 (Table DR2) could be related to persistent sorbed water within the shipboard samples, the deliberate avoidance of veined regions within shipboard protocol (Blackman et al., 2006), unconnected fluid inclusions (Fig. DR4), and/or mineral-mineral scattering. Visual analysis suggests that the majority of pores within the Atlantis Massif samples are likely to be within the measured range (Figs. 1A and 1B), but the larger pores within the Duluth Complex fracture (Fig. 1D) suggest that the total porosities of the fractured samples are probably greater than those reported in Table 1.

**Supplemental Acknowledgements**

Dr. Anette von der Handt (University of Minnesota, UMN) is thanked for assistance with EMP analyses, Dr. Lars Hansen (University of Oxford) is thanked for assistance with SEM-EDS analyses, and Rick Knurr (UMN) is thanked for ICP-OES analyses. XRCT images were acquired in the UMN XRCT laboratory, which was funded by a UMN Infrastructure Investment Initiative Grant.

**Supplemental References**

Abràmoff, M. D., Magalhães, P. J., & Ram, S. J., 2004, Image processing with ImageJ. Biophotonics International, vol. 11 no. 7, p. 36-42.

Bloss, F. D., 1952, Relationship between density and composition in mol percent for some solid solution series. American Mineralogist, vol. 37 no. 11-1, p. 966-981.

Chandler, V. W., 1990, Geologic interpretation of gravity and magnetic data over the central part of the Duluth Complex, northeastern Minnesota. Economic Geology, vol. 85 no. 4, p. 816-829.

Clarkson, Christopher R., N. Solano, R. M. Bustin, A. M. M. Bustin, G. R. L. Chalmers, Lilin He, Yuri B. Melnichenko, A. P. Radliński, and Tomasz Piotr Blach, 2013, Pore structure characterization of North American shale gas reservoirs using USANS/SANS, gas adsorption, and mercury intrusion. Fuel, vol. 103, p. 606-616.

Foster, M.E., and Hudleston, P.J., 1986, “Fracture cleavage” in the Duluth Complex, northeastern Minnesota: Geological Society of America Bulletin, v. 97, p. 85–96.

Hinde, A.L., 2004, PRINSAS–a Windows-based computer program for the processing and interpretation of small-angle scattering data tailored to the analysis of sedimentary rocks: Journal of Applied Crystallography, v. 37, p. 1020–1024, doi:10.1107/S0021889804021260.

Navarre-Sitchler, A.K., Cole, D.R., Rother, G., Jin, L., Buss, H.L., and Brantley, S.L., 2013, Porosity and surface area evolution during weathering of two igneous rocks: Geochimica et Cosmochimica Acta, v. 109, p. 400–413, doi:10.1016/j.gca.2013.02.012.

Radlinski, A.P., Mastalerz, M., Hinde, A.L., Hainbuchner, M., Rauch, H., Baron, M., Lin, J.S., Fan, L., and Thiyagarajan, P., 2004, Application of SAXS and SANS in evaluation of porosity, pore size distribution and surface area of coal: International Journal of Coal Geology, v. 59, p. 245–271, doi:10.1016/j.coal.2004.03.002.

Robie, R.A., and Hemingway, B.S., 1995, Thermodynamic properties of minerals and related substances at 298.15 K and 1 bar ($10^5$ Pascals) pressure and at higher temperatures: U.S. Geological Survey Bulletin 2131, 461 p.